





# optica

## Scan-less confocal phase imaging based on dual-comb microscopy

EIJI HASE,<sup>1,2</sup> TAKEO MINAMIKAWA,<sup>2,3</sup>  TAKAHIKO MIZUNO,<sup>2,3</sup> SHUJI MIYAMOTO,<sup>1</sup> RYUJI ICHIKAWA,<sup>1</sup> YI-DA HSIEH,<sup>2,3</sup> KYUKI SHIBUYA,<sup>1,2</sup> KATSUYA SATO,<sup>3</sup> YOSHIAKI NAKAJIMA,<sup>2,4</sup> AKIFUMI ASAHARA,<sup>2,4</sup> KAORU MINOSHIMA,<sup>2,4</sup> YASUHIRO MIZUTANI,<sup>2,5</sup> TETSUO IWATA,<sup>2,3</sup> HIROTSUGU YAMAMOTO,<sup>2,6</sup> AND TAKESHI YASUI<sup>2,3,\*</sup> 

<sup>1</sup>Graduate School of Advanced Technology and Science, Tokushima University, 2-1, Minami-Josanjima, Tokushima, Tokushima 770-8506, Japan

<sup>2</sup>JST, ERATO, MINOSHIMA Intelligent Optical Synthesizer Project, 2-1, Minami-Josanjima, Tokushima, Tokushima 770-8506, Japan

<sup>3</sup>Graduate School of Technology, Industrial and Social Sciences, Tokushima University, 2-1, Minami-Josanjima, Tokushima, Tokushima 770-8506, Japan

<sup>4</sup>Graduate School of Informatics and Engineering, The University of Electro-Communications, 1-5-1 Chofugaoka, Chofu, Tokyo 182-8585, Japan

<sup>5</sup>Graduate School of Engineering, Osaka University, 2-1, Yamadaoka, Suita, Osaka 565-0871, Japan

<sup>6</sup>Center for Optical Research and Education, Utsunomiya University, 7-1-2, Yoto, Utsunomiya, Tochigi 321-8585, Japan

\*Corresponding author: [yasui.takeshi@tokushima-u.ac.jp](mailto:yasui.takeshi@tokushima-u.ac.jp)

Received 27 December 2017; revised 23 April 2018; accepted 23 April 2018 (Doc. ID 318469); published 16 May 2018

Confocal laser microscopy (CLM) is a powerful tool in life science research and industrial inspection because it offers two-dimensional optical sectioning or three-dimensional imaging capability with micrometer depth selectivity. Furthermore, scan-less imaging modality enables rapid image acquisition and high robustness against surrounding external disturbances in CLM. However, the objects to be measured must be reflective, absorptive, scattering, or fluorescent because the image contrast is given by the optical intensity. If a new image contrast can be provided by the optical phase, scan-less CLM can be further applied for transparent non-fluorescent objects or reflective objects with nanometer unevenness by providing information on refractive index, optical thickness, or geometrical shape. Here, we report scan-less confocal dual-comb microscopy offering a phase image in addition to an amplitude image with depth selectivity by using an optical frequency comb as an optical carrier of amplitude and phase with discrete ultra-multichannels. Our technique encodes confocal amplitude and phase images of a sample onto a series of discrete modes in the optical frequency comb with well-defined amplitude and phase to establish a one-to-one correspondence between image pixels and comb modes. The technique then decodes these images from comb modes with amplitude and phase. We demonstrate confocal phase imaging with milliradian phase resolution under micrometer depth selectivity on the millisecond time-scale. As a proof of concept, we demonstrate the quantitative phase imaging of standing culture fixed cells and the surface topography of nanometer-scale step structures. Our technique for confocal phase imaging will find applications in three-dimensional visualization of stacked living cells in culture and nanometer surface topography of semiconductor objects. © 2018 Optical Society of America under the terms of the [OSA Open Access Publishing Agreement](#)

**OCIS codes:** (180.1790) Confocal microscopy; (180.3170) Interference microscopy; (180.6900) Three-dimensional microscopy; (300.6320) Spectroscopy, high-resolution; (300.6340) Spectroscopy, infrared.

<https://doi.org/10.1364/OPTICA.5.000634>

### 1. INTRODUCTION

Confocal laser microscopy (CLM) [1–3] has been a driving force in life science research and industrial inspection. The confocality enables us to extract a small volume fraction of a sample in the vicinity of a focal point because of a conjugate relationship among a light-source pinhole, a focal point, and a detection pinhole. Therefore, CLM combines high-resolution optical imaging with depth selectivity on the micrometer order, offering two-dimensional (2D) optical sectioning or three-dimensional (3D) imaging capability for a thick sample. Furthermore, 2D spectral encoding [4] enables us to achieve scan-less CLM, in which a 2D image is mapped into a

broad optical spectrum, and then the image-encoded spectrum is captured by an optical spectrum analyzer after giving the confocality. Serial time-encoded amplified microscopy (STEAM) has the potential to further boost the frame rate of CLM up to several megahertz [5]. Such scan-less CLM enables rapid image acquisition and robustness against external disturbances, which will be useful for clinical applications [6–8], endoscopic applications [9,10], or high-throughput surface topography [11,12].

While CLM has found many applications for the use of optical-intensity-based image contrast sensitive to absorption, scattering, reflection, or fluorescence, its range of applications will be further expanded if new image contrast can be given in CLM.

The use of optical phase is an interesting candidate for the new image contrast in CLM because it provides information on refractive index, optical thickness, or geometrical shape and hence visualizes transparent non-fluorescent objects or reflective objects with nanometer unevenness. To date, phase microscopy such as Zernike phase contrast microscopy [13,14], Nomarski differential interference contrast microscopy [14], and quantitative phase microscopy [15–17] has been widely used to visualize thin transparent non-fluorescent specimens with a phase resolution of several to several tens of milliradians, in which phase shifts in light passing through the object are converted to brightness changes in the image by interference. Some phase microscopy techniques can be used to examine the sub-micrometer surface topography of reflective objects. However, the phase value repeats every  $2\pi$  rad (namely, phase wrapping), making it difficult to visualize thick specimens or uneven reflective specimens, both of which introduce phase shifts of more than  $2\pi$  rad, due to the phase wrapping ambiguity. If the phase contrast function can be given in CLM, phase imaging with depth selectivity would be free of the phase wrapping ambiguity. While such confocal phase imaging enables us to visualize a 3D distribution of stacked living cells in culture without any invasiveness for cell engineering, it also enhances the depth resolution of CLM-based surface topography from the micrometer order down to the nanometer order for semiconductor inspection. Confocal phase-sensitive approaches [18–21] are interesting methods to this end because they enable confocal amplitude and phase imaging without the use of pinholes by interfering only light that comes from the confocal volume with a parallel reference beam. The axial resolution of sub-nanometer to nanometer was achieved based on the optical phase information. However, the scanning of focal spot or sample position is still required to obtain the image.

Dual-comb microscopy (DCM) is a new approach to achieving scan-less confocal amplitude and phase imaging by using an optical frequency comb (OFC). An OFC [22–24] is composed of a vast number of discrete, regularly spaced optical frequency modes, and the optical frequency and phase of all OFC modes are secured to a frequency standard by its inherent mode-locking nature and active laser control (see Section 1 of Supplement 1). Although OFCs have been widely used as optical frequency rulers in optical frequency metrology, we here propose a new use for OFCs. First, the OFC acts as an optical carrier of amplitude and phase with a vast number of discrete frequency channels. Second, a physical quantity to be measured is spectrally encoded into OFC modes by dimensional conversion, such as time-to-wavelength [25], space-to-wavelength [26], or polarization-to-wavelength conversion [27]; we call it dimensional-conversion OFC. Third, all data of the physical quantity are decoded all at once from the mode-resolved spectrum of the dimensional-conversion OFC. Based on this concept, the 2D pixels of amplitude and phase images in a sample are separately encoded into a series of discrete modes of the OFC together with the confocality by 2D spectral encoding [Fig. 1(a)]; then, confocal amplitude and phase images are decoded from the mode-resolved amplitude and phase spectra of the image-encoded OFC acquired by dual-comb spectroscopy (DCS) [Fig. 1(b)]. The use of an OFC in 2D spectral encoding enables us to benefit from the well-defined optical phase in scan-less CLM, while establishing a one-to-one correspondence between image pixels and OFC modes for scan-less imaging. Furthermore, DCS [28–31] enables us to rapidly, precisely,

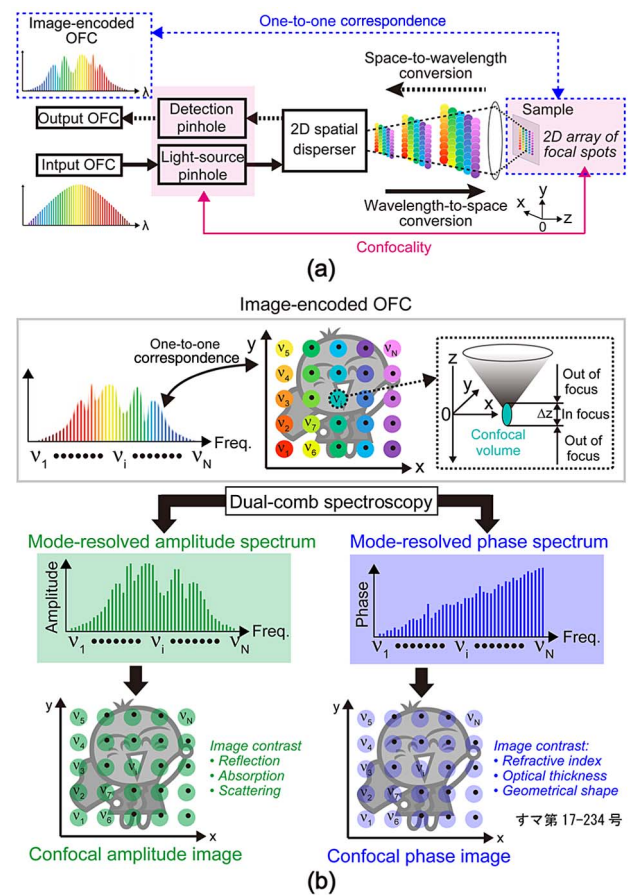


**Fig. 1.** Principle of DCM. (a) Scan-less CLM based on 2D spectral encoding of OFC modes and (b) scan-less confocal amplitude and phase imaging by DCS.

and accurately acquire the mode-resolved amplitude and phase spectra (see Section 1 of Supplement 1). In the following, we acquire a pair of the confocal amplitude image and the confocal phase image in real time, and as a proof-of-principle experiment, we demonstrate the quantitative phase imaging of standing culture fixed cells and the surface topography of a nanometer-scale step-structured sample for scan-less confocal phase imaging.

## 2. METHODS

### A. Principle of Operation

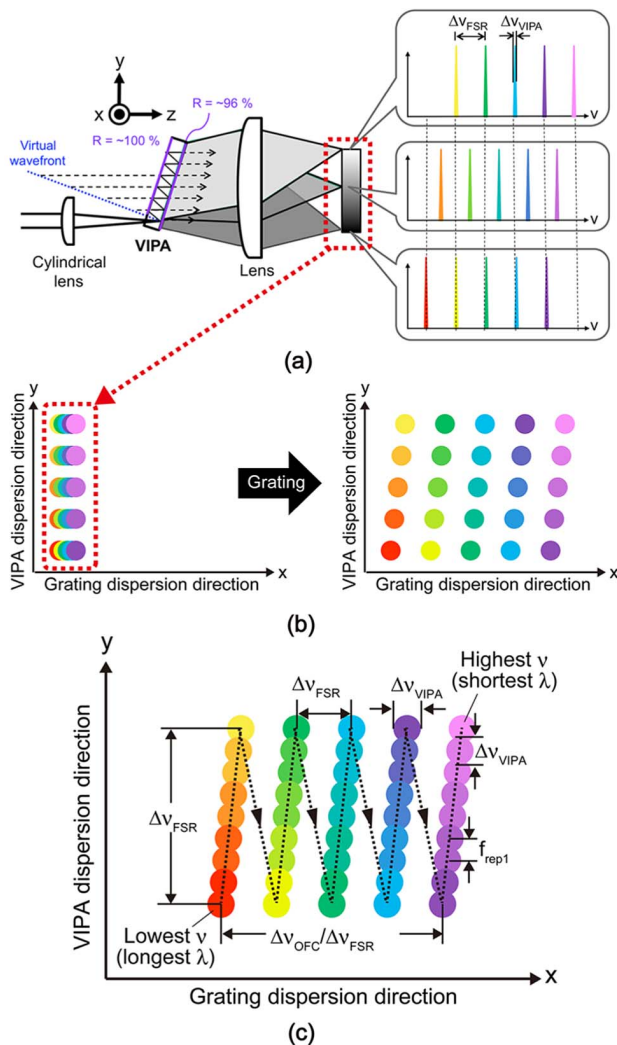
Figure 1(a) shows a principle of scan-less CLM based on 2D spectral encoding of OFC modes. After passing through a light-source pinhole, the optical frequency modes of an input OFC are separately diffracted at a different solid angle along the  $z$  direction by a 2D spatial disperser. The modes are then focused at different positions of a sample in the  $x$ - $y$  plane to form a 2D array of focal spots, corresponding to a 2D spectrograph of the input OFC modes. After being reflected by the sample, the OFC modes are again spatially overlapped with each OFC mode. The resulting image-encoded OFC passes through a detection pinhole, giving the confocality in the full-field image.

Figure 1(b) shows a principle of scan-less confocal amplitude and phase imaging. The 2D array of focal spots on a sample has multiple confocal volumes with a confocal depth resolution  $\Delta z$  in

the  $x$ - $y$  plane due to 2D spectral encoding and confocal optics. DCS of the image-encoded OFC provides amplitude and phase values for those multiple confocal volumes as the mode-resolved amplitude and phase spectra. The confocal amplitude and phase images are reconstructed from the mode-resolved amplitude and phase spectra, respectively, based on the one-to-one correspondence between image pixels and OFC modes.

### B. 2D Spatial Disperser

The 2D spatial disperser [4,5,26,32] was composed of a virtually imaged phased array (VIPA) and a diffraction grating, the dispersion directions of which were orthogonal to each other. VIPA [33] is a tilted Fabry-Perot etalon made of a fused silica plate sandwiched between a 100% reflection coating and a 96% reflection coating except for a light incident window with an anti-reflection coating [Fig. 2(a)]. Analogously to a regular etalon, VIPA shows a transmission spectrum of multiple resonance peaks with a free spectral range of  $\Delta\nu_{\text{FSR}}$  and a resonance transmission linewidth of  $\Delta\nu_{\text{VIPA}}$ ; however, the spectrum of



**Fig. 2.** 2D spatial disperser. (a) Dependence of multiple transmission peaks on the  $y$  position in VIPA with a frequency spacing  $\Delta\nu_{\text{FSR}}$  and a frequency linewidth  $\Delta\nu_{\text{VIPA}}$ . (b) 2D spatial maps of OFC modes before and after passing through a diffraction grating. (c) 2D array of focal spots based on 2D spectral encoding of OFC modes.

the multiple transmission peaks shifts depending on the  $y$  position without a change in  $\Delta\nu_{\text{FSR}}$  due to constructive interference in the tilted etalon configuration [right panel in Fig. 2(a)]. Multiple transmission peaks were spatially overlapped at each  $y$  position, and different groups of multiple transmission peaks were developed along the  $y$  direction [left panel in Fig. 2(b)]. The subsequent diffraction grating was used to develop the spatially overlapped multiple transmission peaks along the  $x$  direction [right panel in Fig. 2(b)].

The VIPA disperses the OFC modes along the vertical ( $y$ ) direction with higher dispersion power due to the deeply tilted, virtual wavefront, while the subsequent grating disperses the spectrum along the horizontal ( $x$ ) direction with lower dispersion power. Therefore, the resulting 2D spectrograph was spatially developed as a zigzag line in the  $x$ - $y$  plane [Fig. 2(c)]. The horizontal dimension of this 2D distribution corresponds to the ratio of the OFC optical bandwidth  $\Delta\nu_{\text{OFC}}$  to  $\Delta\nu_{\text{FSR}}$ , and the vertical dimension depends on  $\Delta\nu_{\text{FSR}}$ . The 2D array of focal spots corresponds to mode-resolved OFC spectrum, and the horizontal and vertical dimensions of the focal spot are limited by  $\Delta\nu_{\text{VIPA}}$ . In the present system described later, since  $\Delta\nu_{\text{VIPA}}$  is larger than a frequency spacing of OFC ( $= f_{\text{rep}}$ ) in the vertical direction, the focal spots partially overlap along the vertical direction. The spacing between horizontally adjacent spots is determined from  $\Delta\nu_{\text{FSR}}$ . Since  $\Delta\nu_{\text{FSR}}$  is larger than  $\Delta\nu_{\text{VIPA}}$ , the focal spots are discrete along the horizontal direction.

### C. Experimental Setup

Figure 3 and Visualization 1 illustrate the experimental setup of DCM to implement the 2D spectral encoding [Fig. 1(a)] and DCS of the image-encoded OFC [Fig. 1(b)]. We used a homemade femtosecond Er-fiber OFC laser (signal OFC laser; center wavelength, 1555 nm; spectral range, 1500–1600 nm; mean output power, 80 mW) for 2D spectral encoding. The carrier-envelope-offset frequency  $f_{\text{ceo1}}$  and a repetition frequency (frequency spacing)  $f_{\text{rep1}}$  were stabilized at 21.4 MHz and 100,387,960 Hz, respectively, by phase-locking to a rubidium frequency standard (Stanford Research Systems, Inc., Sunnyvale, California, USA, FS725; accuracy,  $5 \times 10^{-11}$ ; instability,  $2 \times 10^{-11}$  at 1 s) via a laser control system. After passing through an optical bandpass filter (BPF1; passband, 1538–1562 nm), a light-source

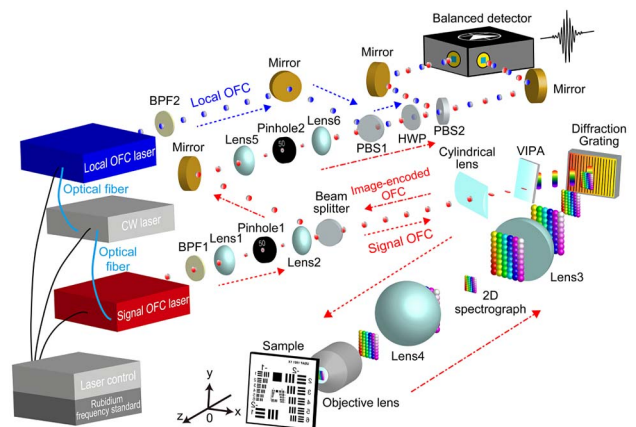


**Fig. 3.** Experimental setup for DCM. See Section 2 for details. Visualization 1 illustrates the propagation of a signal OFC, an image-encoded OFC, and a local OFC in DCM.

pinhole (Pinhole1; diameter, 25  $\mu\text{m}$ ) equipped with a pair of lenses (Lens1 and Lens2; focal length, 50 mm), and a beam splitter, the signal OFC was fed into an optical system for 2D spectral encoding. This optical system was composed of a 2D spatial disperser, a pair of lenses, and an objective lens. The 2D spatial disperser was achieved by combination of VIPA (Light Machinery, Inc., Nepean, Ontario, Canada, OP-6721-6743-8;  $\Delta\nu_{\text{FSR}}$ , 15.1 GHz; finesse, 110;  $\Delta\nu_{\text{VIPA}}$ , 136 MHz) with a diffraction grating (Spectrogon AB, Täby, Sweden, PC 120030  $\times$  30  $\times$  6; groove density, 1200 grooves/mm; efficiency, 90%), which enabled it to disperse the signal OFC modes in 2D space, forming the 2D spectrograph of signal OFC modes. The 2D spectrograph was relayed and then focused onto the sample by a pair of lenses (Lens3 and Lens4; focal length, 150 mm) and the objective lens (dry, numerical aperture, 0.25; working distance, 5.5 mm; focal length, 16 mm). This approach resulted in the formation of the 2D focal spot array of the 2D spectrograph onto a sample. The amplitude and phase images of the sample were encoded onto the 2D spectrograph via reflection, absorption, scattering, or phase change. As the encoded 2D spectrograph passed through the same optical system in the opposite direction, each wavelength component of the spectrograph was spatially overlapped with each other again as an image-encoded OFC. After being reflected by the beam splitter and passing through a detection pinhole (Pinhole2; diameter, 25  $\mu\text{m}$ ) equipped with a pair of lenses (Lens5 and Lens6; focal length, 50 mm), the image-encoded OFC was fed into the experimental setup of the DCS.

The DCS setup incorporated another homemade femtosecond Er-fiber OFC laser (local OFC laser; center wavelength, 1555 nm; spectral range, 1530–1585 nm; mean output power, 80 mW;  $f_{\text{ceo2}} = 21.4$  MHz;  $f_{\text{rep2}} = 100,389,194$  Hz). The local OFC laser had an intra-cavity electro-optical modulator for laser control [34] and was tightly and coherently locked to the signal OFC laser with a constant frequency offset  $\Delta f_{\text{rep}} (= f_{\text{rep2}} - f_{\text{rep1}} = 1234$  Hz) using a narrow-linewidth continuous-wave (CW) laser (Redfern Integrated Optics, Inc., Santa Clara, California, USA, PLANEX; center wavelength, 1550 nm; FWHM, <2.0 kHz) for an intermediate laser [35,36]. This locking enabled us to coherently accumulate interferograms obtained with DCS [37,38] and hence to enhance the signal-to-noise ratio (SNR). The image-encoded OFC was spatially overlapped with the local OFC by using a polarization beam splitter (PBS1). The interferogram was detected by a combination of a half-wave plate (HWP), another polarization beam splitter (PBS2), and a balanced detector (Newport Corp., Irvine, California, USA, 1617-AC-FS; wavelength, 900–1700 nm; bandwidth, 40 kHz to 800 MHz). The detected electrical signal was acquired within 810  $\mu\text{s}$  using a digitizer (National Instruments Corp., Austin, Texas, USA, NI PCI-5122; sampling rate, 100,389,194 samples/s; number of sampling points, 81,353; resolution, 14 bit). The sampling clock signal was synchronized with  $f_{\text{rep2}}$ . The acquired signal corresponded to an interferogram signal with a time window of 9.96 ns ( $= 1/f_{\text{rep1}}$ ) and a sampling interval of 122 fs ( $= 1/f_{\text{rep1}} - 1/f_{\text{rep2}}$ ).

A Fourier transform of the acquired interferogram signal gives the mode-resolved amplitude and phase spectra of the image-encoded OFC with a frequency sampling interval of  $f_{\text{rep1}}$  ( $= 100,387,960$  Hz). Before decoding the confocal amplitude image, a normalized amplitude spectrum was obtained by using the amplitude spectrum of no-image-encoded OFC as a

reference to eliminate the influence of the spectral shape of the signal OFC. Similarly, we subtracted the phase spectrum of the no-image-encoded OFC from the phase spectrum of the image-encoded OFC to eliminate the influence of the initial phase in the signal OFC. Then, each data plot of the normalized mode-resolved amplitude and phase spectra was spatially mapped for the confocal amplitude and phase images based on the zigzag mapping of 2D spectral encoding [Fig. 2(c)].

### 3. RESULTS

#### A. Confocal Amplitude and Phase Imaging of Test Chart

We used a commercialized 1951 USAF resolution test chart with a positive pattern (Edmond Optics, Barrington, New Jersey, USA, #38-257; spatial frequency, 1.00 lp/mm  $\sim$  228 lp/mm) for the first sample [Fig. 4(a)]. Positive patterns were fabricated by vacuum-depositing a durable chromium coating on a float glass substrate (thickness: 1.5 mm) as a reflective film. The reflectivity of the chromium film and the glass substrate was 45% and 10%, respectively. The chromium film caused the 2D distribution of both the reflectivity and the phase change corresponding to the chart patterns.

The test chart was placed at the focal position ( $z = 0$   $\mu\text{m}$  in Fig. 3) as the sample. We acquired temporal waveforms of an interferogram at 1234 Hz, accumulated 100 temporal waveforms (data acquisition time: 81 ms), and performed a Fourier transform of the accumulated signal. We then obtained the mode-resolved amplitude and phase spectra of the no-image-encoded OFC [Figs. 4(b) and 4(c)] and the image-encoded OFC [Figs. 4(d) and 4(e)] for the test chart. The no-image-encoded OFC and the image-encoded OFC were obtained by irradiating the signal OFC onto the solid coating area and the pattern coating area of the test chart [Fig. 4(a)]. The pattern coating area includes Element 2 in Group 4 with spatial frequency of 17.95 lp/mm and Element 1 in Group 5 with spatial frequency of 32.00 lp/mm. All spectra range from 192.8 to 194.3 THz, and include 15,000 OFC modes from the spectral range of 1.5 THz and the OFC mode spacing of 100 MHz. The fine structure inside the amplitude spectra reflects the resonance transmission peaks of VIPA. The amplitude spectrum of the image-encoded OFC was significantly modulated, compared with that of the no-image-encoded OFC. On the other hand, the phase value in Figs. 4(c) and 4(e) varies within the range of  $\pm\pi$  due to phase wrapping. Normalized amplitude and phase spectra were calculated by using mode-resolved amplitude and phase spectra of the no-image-encoded OFC and the image-encoded OFC (see Section 2), as shown in Figs. 4(f) and 4(g). Unevenness in the amplitude and phase spectra reflects the 2D distribution of the reflectivity and the phase change in the test chart, respectively. Their enlarged spectra are shown in Figs. 4(h) and 4(i). In Fig. 4(h), high values reflect high reflectivity or low transmission at the reflective coating area whereas low ones correspond to low reflectivity or high transmission at the uncoated glass surface, respectively. In Fig. 4(i), the gentle change of phase value reflects the phase distribution, whereas noise periodically appears as sharp dips at frequencies of low amplitude in Fig. 4(h).

By using the 2D spatial disperser, all OFC modes with the lowest optical frequency  $\nu$  (longest wavelength  $\lambda$ ) to the highest  $\nu$  (shortest  $\lambda$ ) are spatially developed as a zigzag line in the  $x$ - $y$

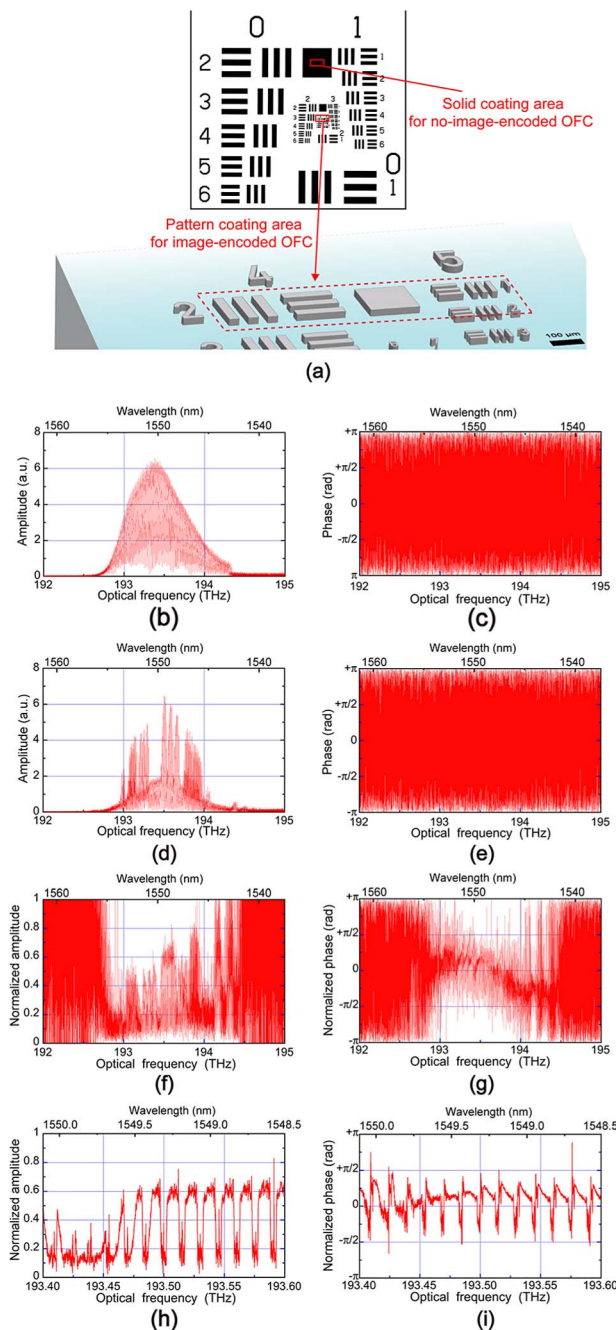


**Fig. 4.** Mode-resolved amplitude and phase spectra of OFCs. (a) Schematic drawing of 1951 USAF resolution test chart with positive pattern. Mode-resolved (b) amplitude and (c) phase spectra of the no-image-encoded OFC. Mode-resolved (d) amplitude and (e) phase spectra for spectral decoding of confocal amplitude and phase images, and their enlarged spectra of (h) amplitude and (i) phase.

plane, enabling a one-to-one correspondence between image pixels and OFC modes [Fig. 2(c)]. Following this correspondence, the amplitude and phase values of OFC modes in the normalized mode-resolved amplitude and phase spectra [Figs. 4(f) and 4(g)] were spatially mapped as the confocal amplitude and phase images [Figs. 5(a) and 5(b)]. The 12,382 OFC modes within the spectral range of 192.9–194.1 THz were extracted and then converted

into 12,382 pixels (= 82 × 151 pixels) in these images. Patterns of Element 2 in Group 4 and Element 1 in Group 5 were clearly confirmed in both images. For reference, we measured a transmission image of the same pattern using an infrared camera (Allied Vision Technologies GmbH, Stadroda, Germany, Goldeye P-008 SWIR Cool, Peltier cooling; pixel number, 320 pixels by 256 pixels; pixel size, 30 μm by 30 μm; resolution, 14 bit) placed behind the test chart [Fig. 5(c)]. Although the image distortion was somewhat retained due to the zigzag scanning in the 2D spectral encoding [Fig. 2(c)], the confocal amplitude and phase images were in good agreement with the camera image. The possible scan rate remained at 12.34 Hz in Figs. 5(a) and 5(b) due to the signal accumulation of 100 interferogram signals; however, we can still improve the image acquisition rate up to 1234 Hz by reducing the number of signal accumulation. To demonstrate the fast imaging capability of the proposed system, we acquired a series of confocal amplitude and phase images of the test chart moving in the *x*-*y* plane without signal accumulation (image acquisition rate = 1234 Hz; Visualization 2). Although the obtained amplitude and phase images have lower contrast than those in Fig. 5, the moving test chart was just about discernible.

Note that the image contrast is generated by different mechanisms: reflectivity for the confocal amplitude image, phase

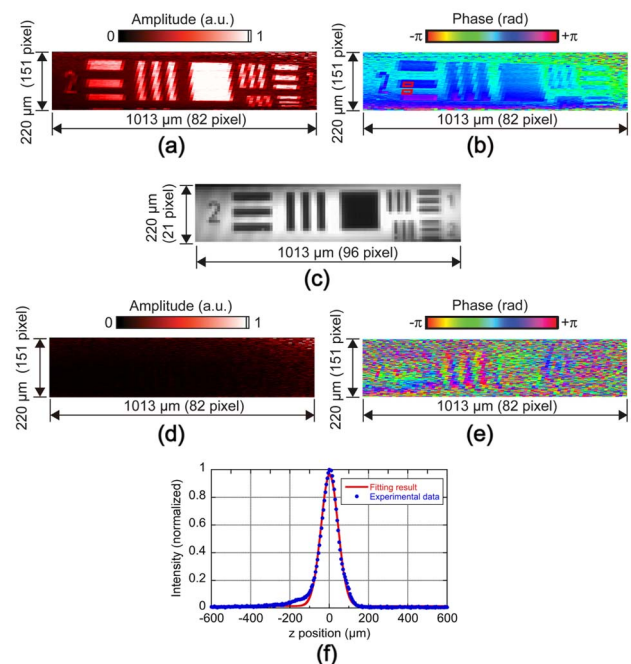


**Fig. 5.** Confocal amplitude and phase images. (a) Confocal amplitude image and (b) confocal phase image of the test chart placed at the focal position ( $z = 0 \mu\text{m}$ ; image acquisition time, 81 ms). The relative phase was calculated by using a phase value at a certain pixel of the image as a reference. Visualization 2 shows a series of confocal amplitude and phase images of the test chart moving in the *x*-*y* plane without signal accumulation (image acquisition time, 0.81 ms; image acquisition rate, 1234 Hz). (c) Transmission image of the test chart acquired by an infrared camera. (d) Confocal amplitude image and (e) confocal phase image of the test chart placed out of focus ( $z = +215 \mu\text{m}$ ; image acquisition time, 81 ms). Visualization 3 shows the changes in the confocal amplitude and phase images when the sample position is moved along the *z* direction. (f) Confocal profile of the amplitude value with respect to the *z* position, which is calculated from the amplitude image in Visualization 3.

change for the confocal phase image, and transmittance for the camera image. The contrast in the confocal amplitude image is the inverse of that in the camera image due to a relationship between reflection and transmission. The contrast in the confocal phase image was due to the phase change resulting from the presence or absence of the reflective chromium film on the glass for a positive pattern [Fig. 4(a)]. Since the mean and standard deviation of the relative phase distribution were  $-0.56 \pm 0.02$  rad in the coating region [see an upper red box in Fig. 5(b)] and  $0.38 \pm 0.05$  rad in the no-coating region [see a lower red box in Fig. 5(b)], the phase change between them was determined to be  $0.94 \pm 0.06$  rad. This phase change reflects not only the geometrical thickness of the reflective chromium film but also the difference between the complex indices of refraction of the chromium film and the float glass.

To confirm the confocality, we measured the confocal amplitude and phase images of the test chart positioned at  $z$  of  $+215 \mu\text{m}$  for out-of-focus images [Figs. 5(d) and 5(e)]. The chart pattern disappeared completely in the amplitude image; in the phase image, it was buried in the surrounding region, which filled with random noise, because the phase noise appears as random values within the range of  $\pm\pi$  rad. In addition, we acquired a series of confocal amplitude and phase images obtained with the test chart moving along the  $z$  direction from  $-215$  to  $+215 \mu\text{m}$  (Visualization 3). When the test chart was moved out of focus, the image contrast significantly decreased in both images. In this way, the confocality was clearly confirmed in both the phase image and amplitude image. From the amplitude images, we calculated the amplitude values on the pattern region of the test chart with respect to the  $z$  position [blue plots in Fig. 5(f)], which corresponds to the confocal depth profile of the proposed DCM. From the curve fitting analysis with a Gaussian function [red line in Fig. 5(f)], the confocal depth resolution  $\Delta z$  was determined to be  $61 \mu\text{m}$  when it was defined as the full width at half maximum (FWHM) in the depth profile.

## B. Quantitative Phase Imaging of Standing Culture Fixed Cells

To demonstrate a potential bio-imaging application, we applied the confocal phase imaging to standing culture fixed cells. We used the mouse fibroblast cell line NIH3T3, which was provided by the RIKEN-BRC through the National Bio-Resource Project of the Ministry of Education, Culture, Sports, Science and Technology (MEXT), Japan. The medium for cell culturing was D-MEM (Wako pure chemical industries, Ltd.) supplemented with 10% calf serum and 1% penicillin and streptomycin solutions (100 U/ml and 100  $\mu\text{g}/\text{ml}$ , respectively). A substrate for cell adhesion was made of glass plate ( $20 \times 13 \text{ mm}$ ,  $t = 1 \text{ mm}$ ) coated with thin gold film (thickness: 50 nm) for observation at a reflection geometry (DCM) and a transmission geometry (phase contrast microscopy). The glass plate was sterilized by immersing in 70% EtOH for 20 min. After 3 times rinse with Dulbecco's Phosphate Buffered Saline (DPBS), its surface was then coated with fibronectin solution ( $20 \mu\text{g}/\text{cm}^2$ ) (Wako Pure Chemical Industries, Ltd.) for 1 h to enhance the cell adhesion. Then the glass plate was rinsed twice with DPBS and placed in a well plate with a diameter of 35 mm. After the cells were seeded onto the glass plate, they were cultured in the  $\text{CO}_2$  incubator. We performed standing culture of the cells for 12 h, and then fixed them with 4% paraformaldehyde.

Before performing DCM, we first visualized this NIH3T3 cell sample by phase contrast microscopy (dry, numerical aperture, 0.13; magnification, 4). Figure 6(a) shows the phase contrast image of the NIH3T3 cell sample, indicating the sparse distribution of cells with a density of 66 cells/ $\text{mm}^2$ . We next visualized the NIH3T3 cell sample by DCM. Figures 6(b) and 6(c) respectively show the confocal amplitude and phase images of the NIH3T3 cell sample. The transparency of the sample makes it difficult to give the contrast in the confocal amplitude image. In contrast, cells were visualized in the confocal phase image due to the refractive-index-based contrast, although its field of view did not coincide with that in the phase contrast image. A small difference of refractive index between the NIH3T3 cell and the medium and insufficient spatial resolution makes its contrast low. Nevertheless, sparse distribution of NIH3T3 cell was confirmed again. The  $x$ - $y$  spatial dimension of each cell in the confocal phase image is in good agreement with that in the phase contrast image. It is important to note that a main advantage of DCM over phase contrast microscopy is in imparting confocality to the quantitative phase image. The achieved image acquisition rate ( $= 12 \text{ Hz}$ ) will be sufficient for *in vivo* monitoring of structural changes of the cell membrane, cytoskeleton, and nucleus in living cells. If the image acquisition rate is further increased, the transient cell response to external stimulation will be further visualized.

## C. Surface Topography of Nanometer-Scale Three-Step Structure

We next applied the confocal phase imaging to the nanometer-scale surface topography of a reflective object to demonstrate a potential industrial inspection application. For a sample, we fabricated a nanometer-scale three-step structure with different heights ( $h_1$ ,  $h_2$ , and  $h_3$ ) [Fig. 7(a)] using the following procedure. A polymethyl methacrylate (PMMA) solution was spin-coated onto the surface of a silicon substrate. A portion of the formed PMMA film was exposed to an electron beam, and the exposed region was then removed by a developing solution. Silver film formed on both the bare silicon and the remaining PMMA film by a vacuum thermal evaporation method. Only the silver film on the PMMA film was lifted off by a peeling liquid. By repeating this procedure while changing the exposed region, the step structure with different nanometer-scale heights was prepared on the silicon substrate. Finally, a thin gold film was deposited on all surfaces of this step-structured sample by a vacuum thermal evaporation method.

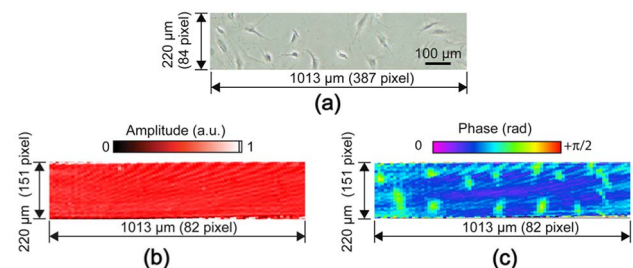


**Fig. 6.** Quantitative phase imaging of NIH3T3 cells. (a) Phase contrast image, (b) confocal amplitude image, and (c) confocal phase image of the sample placed at the focal position ( $z = 0$ ). The image acquisition time of the confocal amplitude and phase images was 81 ms.

Figures 7(b) and 7(c) respectively show the confocal amplitude and phase images of a region of interest [ROI 1, indicated by blue dashed box in Fig. 7(a)] in this sample, in which the edges of the step structures are indicated by black dashed lines. In the amplitude image of the step structure, the steps have similar contrast because of small differences of reflectivity between different surfaces. In addition, the confocality could not discriminate such small step differences due to insufficient depth selectivity [Fig. 5(f)]. However, the phase image clearly visualizes the step structure because the image contrast is based on phase changes, which are sensitive to nanometer-scale geometrical shapes. The 2D distribution of relative height  $H(x, y)$  of the sample surface is given by

$$H(x, y) = \frac{1}{2} \frac{\phi(x, y)}{2\pi} \lambda = \frac{\lambda}{4\pi} \phi(x, y), \quad (1)$$

where  $\lambda$  is a typical wavelength of OFC modes ( $= 1550$  nm), and  $\phi(x, y)$  is the phase image. Therefore, the confocal phase image enabled us to calculate the 3D shape of the sample. Figure 7(d) and Visualization 4 show the 3D shape of another region of interest [ROI 2, indicated by white dashed box in Figs. 7(a) and 7(c)] in this sample. We determined the height of each step to be  $317 \pm 12$  nm for  $h_1$ ,  $122 \pm 13$  nm for  $h_2$ , and  $51 \pm 18$  nm for  $h_3$ .

To validate those values, a commercialized atomic force microscope (AFM, Olympus Corp., Shinjuku, Tokyo, Japan, OLS3500-PTU; depth resolution  $= 55.6$   $\mu\text{m}$ ) was used in the tapping mode. While a silicon cantilever with a sharpened tetrahedral tip (Olympus Corp., Shinjuku, Tokyo, Japan,

OMCL-AC160TN-C3; tip radius, 7 nm; resonance frequency, 300 kHz) was driven to oscillate up and down at its resonance frequency, the sample position was scanned at a 58.6 nm step within the range of 30 and 0.586  $\mu\text{m}$  across the step structure along the  $x$  and  $y$  directions, respectively. The surface profile was determined to be  $315.4 \pm 12.1$  nm for  $h_1$ ,  $122.5 \pm 11.6$  nm for  $h_2$ , and  $50.5 \pm 10.4$  nm for  $h_3$ , respectively; these values were in good agreement with those measured with DCM.

## 4. DISCUSSION

The key achievement of DCM is scan-less confocal phase imaging. We first discuss the phase resolution in the present confocal phase imaging. The phase resolution is defined as the phase noise of the signal, which depends on the robustness of the optical system to external disturbance (vibration, air turbulence, etc.), the timing jitter between the signal OFC and the local OFC, and/or the signal SNR. We acquired 100 repetitive confocal phase images and then calculated the standard deviation of the phase values at the same pixel to provide the phase resolution. The resulting phase resolution was 0.028 rad, which was reasonably reflected in the confocal phase imaging of the test chart [Fig. 5(b)]. The phase resolution of 0.028 rad within the full phase range of  $2\pi$  rad corresponds to the phase resolving power of  $1/224 (= 0.028/2\pi)$ . This phase resolving power is comparable to that of conventional phase microscopy; however, imparting confocality to the quantitative phase image is a considerable advantage over phase microscopy. If the confocal phase imaging is applied for the surface topography demonstrated in Fig. 7, this phase resolving power leads to a phase depth resolution of 3.5 nm from Eq. (1). This depth resolution is 2–3 orders of magnitude smaller than that of existing intensity-based CLM (typically, a few micrometers).

We next discuss the confocal depth resolution  $\Delta z$  in the confocal phase imaging. The experimental  $\Delta z$  value was 61  $\mu\text{m}$  [Fig. 5(f)]. The theoretical  $\Delta z$  value with the relatively large confocal pinhole used here is given by

$$\Delta z = \frac{0.88\lambda}{n - \sqrt{n^2 - \text{NA}^2}} = \frac{0.88 \times 1.550}{1 - \sqrt{1^2 - 0.25^2}} = 43 \mu\text{m}, \quad (2)$$

where  $\lambda$  is a typical wavelength of OFC modes,  $n$  is the refractive index of the medium, and NA is the numerical aperture of the objective lens. The experimental and theoretical  $\Delta z$  values were somewhat different because the 2D spectrograph of the OFC did not fully fill the entrance pupil of the objective lens in the present experimental setup (Fig. 3).

Here, we consider the relationship between the confocal depth resolution and the OFC wavelength from the viewpoint of a surface topographic application. The present DCM has a theoretical  $\Delta z$  value larger than the half  $\lambda$  value ( $= 775$  nm). The inconsistency between  $\Delta z$  and  $\lambda/2$  limits the measurable height range because the phase wrapping still occurs every  $2\pi$  rad, corresponding to  $\lambda/2$ , within the range of  $\Delta z$  [see Eq. (1)]. Therefore, the measurable height range is limited within  $\lambda/2$  to avoid the phase wrapping ambiguity. Although the phase unwrapping process can expand this range beyond  $\lambda/2$ , its application is limited to a smooth or even surface. Significantly, the phase wrapping ambiguity, which is always an obstacle in any phase imaging, can essentially be solved by matching  $\Delta z$  with  $\lambda/2$  in DCM because the confocality suppresses the phase wrapping. Fortunately, there is still sufficient space to decrease  $\Delta z$ . For example, if an oil-immersion, high-NA objective lens ( $\text{NA}$ , 1.4;  $n$ , 1.4) is used

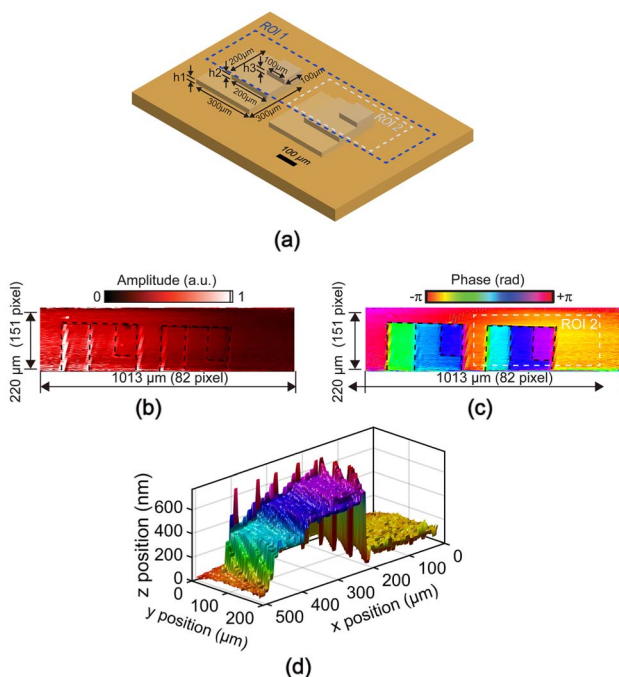


**Fig. 7.** Surface topography based on confocal phase imaging. (a) Schematic drawing of a nanometer-scale three-step structure sample. (b) Confocal amplitude image and (c) confocal phase image of the sample placed at the focal position ( $z = 0$ ). The image acquisition time was 81 ms. (d) 3D image of the sample calculated from the confocal phase image. Visualization 4 shows the movie of the 3D shape from various angles of vision.

in a sufficiently small confocal pinhole, the following theoretical  $\Delta z$  value can be achieved:

$$\Delta z = \frac{0.68\lambda}{n - \sqrt{n^2 - \text{NA}^2}} = \frac{0.68 \times 1.550}{1.4 - \sqrt{1.4^2 - 1.4^2}} = 0.75 \mu\text{m}. \quad (3)$$

The consistency between  $\Delta z$  and  $\lambda/2$  seamlessly connects the phase imaging with the confocal imaging, significantly enhancing the dynamic range of depths from nanometer to micrometer to millimeter scales. This wide dynamic range of depths is the ultimate goal of confocal phase imaging for surface topographic applications.

We next evaluate the lateral resolution. The confocal amplitude and phase images of the chart patterns with spatial frequencies of 17.95 and 32.00 lp/mm were visualized at sufficient spatial resolution [Figs. 5(a) and 5(b)]. To investigate the limit of the imaging performance, the experimental value of the spatial resolution was evaluated by a knife-edge test. The line profile across an edge of the square pattern region was extracted along the  $x$  and  $y$  directions in the confocal amplitude image [Fig. 5(a)], and then the curve fitting analysis with an error function was performed to the line profile. The resulting spatial resolution was 12.4  $\mu\text{m}$  for the  $x$  direction and 2.5  $\mu\text{m}$  for the  $y$  direction.

Theoretical spatial resolution in 2D spectral encoding is estimated from the relationship between the dimension of the focal spot and the spacing between adjacent focal spots [39]. The theoretical value of the spatial resolution in the  $x$  direction ( $\Delta x$ ) depends on the horizontal spot spacing rather than on the horizontal dimension of the focal spot due to the discrete distribution along the  $x$  direction [Fig. 2(c)]. This value is given by

$$\Delta x = \left( f \frac{d\theta_g}{d\lambda} \right) \Delta\lambda_{\text{FSR}} = 11.4 \mu\text{m}, \quad (4)$$

where  $f$  is the focal length of the objective lens,  $d\theta_g/d\lambda$  is the angular dispersion of the diffraction grating, and  $\Delta\lambda_{\text{FSR}}$  is one FSR of the VIPA in wavelength. On the other hand, the theoretical value of the spatial resolution in the  $y$  direction ( $\Delta y$ ) depends on the vertical dimension of the focal spot due to the spatially overlapped distribution along the  $y$  direction [Fig. 2(c)] and is given by

$$\Delta y = \left( f \frac{d\theta_{\text{VIPA}}}{d\lambda} \right) \Delta\lambda_{\text{VIPA}} = 2.0 \mu\text{m}, \quad (5)$$

where  $d\theta_{\text{VIPA}}/d\lambda$  is the angular dispersion of the VIPA, and  $\Delta\lambda_{\text{VIPA}}$  is the spectral linewidth of the transmission resonance of the VIPA in wavelength. The overlapping focal spots in the  $y$  direction smear out the pixels but increase the image SNR due to full use of OFC modes. These theoretical values of spatial resolution are in good agreement with the experimental value of that.

The fast imaging capability is an important characteristic of the scan-less CLM. The image acquisition rate in the present system is determined by the measurement rate of DCS, which is equal to the difference in frequency spacing between dual OFCs (= 1234 Hz) and the number of signal integrations. Without the signal accumulation, we achieved the scan rate of 1234 Hz in Visualization 2. This scan rate is higher than that in the previous scan-less CLM using an optical spectrum analyzer [4], although it could not reach that of a STEAM camera [5]. A kilohertz frame rate will be sufficient for most CLM applications. There is still space to improve the image SNR at kilohertz frame rate. To this

end, the use of OFC with higher  $f_{\text{rep}}$  and higher total power is a simple way to increase the power of each OFC mode. The spectral bandwidth of OFC should be optimized because it was largely filtered to avoid the aliasing in DCS by BPF1. The narrower-bandwidth OFC that does not exceed the bandwidth to avoid aliasing in DCS would not require BPF1 and hence will largely improve the SNR. Use of the lower  $\Delta f_{\text{rep}}$  will contribute to improving the SNR if the timing jitter between dual-comb lasers is sufficiently suppressed. Also, confocal phase-sensitive approaches [18–21] may enable the DCM system without the use of the detection pinhole because only the beam that comes from the multiple focal points of the signal OFC is interfered with a properly collimated beam of the local OFC. This leads to increase of the SNR due to no loss of signal OFC light in the pinhole. Furthermore, optical post-amplification of the image-encoded OFC by an erbium-doped fiber amplifier (EDFA) will be powerful although gain and phase profiles in EDFA have to be characterized beforehand for calibration of amplitude and phase spectra.

Finally, we discuss the practicability of DCM. Compared with intensity-based CLM [1–3], the scan-less CLM [4,5], or the phase-sensitive CLM [18–21], the use of dual-stabilized OFCs might hamper the practical use of DCM from the viewpoints of ease of implementation and cost. In DCM, OFC is not used as an optical frequency ruler but instead as an optical carrier of amplitude and phase with discrete ultra-multichannel. In this case, strict stabilization control of the OFC is not always indispensable if only the mode-resolved amplitude and phase spectra of the image-encoded OFC can be acquired. Recently, single-cavity dual-comb lasers were developed by multiplexing mode-locking operations in the wavelength [40], polarization [41], or propagation directions [42,43]. Because they did not need dual cavities and their stabilization control, they attracted attention as a low-cost, low-complexity, dual-comb laser for DCS. If these lasers are implemented in DCM together with adaptive sampling DCS [44], its practicability will be greatly enhanced and will be comparable to existing CLM.

## 5. CONCLUSION AND OUTLOOK

We have demonstrated the successful introduction of optical-phase-based image contrast to scan-less CLM by using the dimensional-conversion OFC. Scan-less confocal phase imaging, which gives information on refractive index, optical thickness, or geometrical shape with the depth selectivity, will further expand the range of measurable objects in CLM and will open the door for new CLM applications. The proposed DCM also shows a possibility to seamlessly link scan-less CLM with phase microscopy by matching the confocal depth resolution with a half wavelength of an OFC, offering phase imaging without phase wrapping ambiguity within the wide axial range from micrometers to millimeters. The proposed DCM will greatly enhance the applicability of CLM to wide-dynamic-range surface topography for the industrial inspection of semiconductor objects. Another interesting application of DCM is in non-destructively inspecting optical components and devices such as micro optics or fiber optics by using the image contrast of refractive index or optical thickness. Furthermore, DCM will be a powerful tool in life science research such as 3D imaging of stacked living cells in culture if the lateral resolution and confocal depth resolution are further reduced to sub-micrometer.



The present DCM was applied for specularly reflecting targets; however, it will be applicable for diffusely reflecting targets. Although the diffuse reflection reduces the coherent component of the signal OFC light that can interfere with the local OFC light, this approach still works for such targets as long as the coherent component remains and the resulting interferogram can be acquired by DCS. Note that too strong diffuse reflection might break one-to-one correspondence between a 2D array of focal spots and OFC modes. Also, it might be interesting to compare the present DCM with DCS single-pixel imaging (DCS-SPI) [45] because both methods are based on DCS, benefit from scan-less imaging, and enable amplitude and phase imaging. While DCM achieved scan-less imaging at the cost of spectral information by 2D spectral encoding, the kilohertz scan rate was achieved together with the confocality. On the other hand, DCS-SPI realizes the scan-less imaging by use of optical spatial coding on a sample with single-channel detection. While DCS-SPI enables ultrahigh-density hyperspectral amplitude and phase imaging, its image acquisition rate is much slower than that of DCS due to repetitive coding of different optical spatial masks by a spatial light modulator. Also, the optical spatial coding hampers us in combining DCS-SPI with the confocality. In this way, DCM and DCS-SPI, respectively, have unique features complementary to each other, and will find different applications.

Finally, the concept of dimensional-conversion OFC will bring great benefits not only to CLM but also to other optical metrologies by use of a wide variety of dimensional conversion [25–27] due to no crosstalk by discrete mode distribution, collective data acquisition by the sufficient number of modes, infinitesimal sampling width by ultra-narrow mode linewidth, and regular sampling interval by stable  $f_{\text{rep}}$ . Too discrete sampling ratio can be relaxed by spectral interleaving [46] or temporal interleaving [47]. Such a concept will expand the application scope of OFCs beyond their current use based on optical frequency rulers and will extend to various optical metrology and instrumentation.

**Funding.** Exploratory Research for Advanced Technology (ERATO), Japanese Science and Technology Agency (MINOSHIMA Intelligent Optical Synthesizer Project, JPMJER1304); Japan Society for the Promotion of Science (JSPS) (15H02026, 26246031); Mazda Foundation.

**Acknowledgment.** The authors acknowledge Dr. Toshihiro Okamoto and Mr. Shun Kamada of Tokushima University, Japan, for their help in the sample preparation and evaluation. The authors also acknowledge Ms. Shoko Lewis and Ms. Natsuko Takeichi of Tokushima University, Japan, for their help in the preparation of the manuscript. T. Y., H. Y., and K. M. conceived the project. E. H., S. M., Tak. Miz., R. I., Y.-D. H., and Kyu. Shi. performed the experiments and/or analyzed the data. Y. N. and A. A. contributed to the dual-comb sources. Kat. Sat. prepared cell samples. E. H. and T. Y. wrote the manuscript. Tak. Min., Y. M., and T. I. discussed the results and commented on the manuscript.

See [Supplement 1](#) for supporting content.

## REFERENCES

- P. Davidovits and M. D. Egger, "Photomicrography of corneal endothelial cells *in vivo*," *Nature* **244**, 366–367 (1973).
- G. J. Brakenhoff, P. Blom, and P. Barends, "Confocal scanning light microscopy with high aperture immersion lenses," *J. Microsc.* **117**, 219–232 (1979).
- C. J. Sheppard and D. M. Shotton, *Confocal Laser Scanning Microscopy* (BIOS Scientific, 1997).
- K. K. Tsia, K. Goda, D. Capewell, and B. Jalali, "Simultaneous mechanical-scan-free confocal microscopy and laser microsurgery," *Opt. Lett.* **34**, 2099–2101 (2009).
- K. Goda, K. K. Tsia, and B. Jalali, "Serial time-encoded amplified imaging for real-time observation of fast dynamic phenomena," *Nature* **458**, 1145–1149 (2009).
- M. Rajadhyaksha, S. González, J. M. Zavislan, R. R. Anderson, and R. H. Webb, "*In vivo* confocal scanning laser microscopy of human skin II: advances in instrumentation and comparison with histology," *J. Invest. Dermatol.* **113**, 293–303 (1999).
- M. T. Tilli, M. C. Cabrera, A. R. Parrish, K. M. Torre, M. K. Sidawy, A. L. Gallagher, E. Makariou, S. A. Polin, M. C. Liu, and P. A. Furth, "Real-time imaging and characterization of human breast tissue by reflectance confocal microscopy," *J. Biomed. Opt.* **12**, 051901 (2007).
- A. Vogel, J. Noack, G. Hüttman, and G. Paltauf, "Mechanisms of femtosecond laser nanosurgery of cells and tissues," *Appl. Phys. B* **81**, 1015–1047 (2005).
- G. J. Tearney, M. Shishkov, and B. E. Bouma, "Spectrally encoded miniature endoscopy," *Opt. Lett.* **27**, 412–414 (2002).
- C. Pitris, B. E. Bouma, M. Shishkov, and G. J. Tearney, "A GRISM-based probe for spectrally encoded confocal microscopy," *Opt. Express* **11**, 120–124 (2003).
- B. V. R. Tata and B. Raj, "Confocal laser scanning microscopy: applications in material science and technology," *Bull. Mater. Sci.* **21**(4), 263–278 (1998).
- D. Lellouchi, F. Beaudoin, C. Le Touze, P. Perdu, and R. Desplats, "IR confocal laser microscopy for MEMS technological evaluation," *Microelectron. Reliab.* **42**, 1815–1817 (2002).
- F. Zernike, "Phase contrast, a new method for the microscopic observation of transparent objects," *Physica* **9**, 686–698 (1942).
- D. B. Murphy, *Fundamentals of Light Microscopy and Electronic Imaging* (Wiley, 2002).
- H. Iwai, C. Fang-Yen, G. Popescu, A. Wax, K. Badizadegan, R. R. Dasari, and M. S. Feld, "Quantitative phase imaging using actively stabilized phase-shifting low-coherence interferometry," *Opt. Lett.* **29**, 2399–2401 (2004).
- C. J. Mann, L. Yu, C. M. Lo, and M. K. Kim, "High-resolution quantitative phase-contrast microscopy by digital holography," *Opt. Express* **13**, 8693–8698 (2005).
- G. Popescu, T. Ikeda, R. R. Dasari, and M. S. Feld, "Diffraction phase microscopy for quantifying cell structure and dynamics," *Opt. Lett.* **31**, 775–777 (2006).
- R. L. Jungeman, P. C. D. Hobbs, and G. S. Kino, "Phase sensitive scanning optical microscope," *Appl. Phys. Lett.* **45**, 846–848 (1984).
- T. Wilson and C. W. Shepard, *Theory and Practice of Scanning Optical Microscopy* (Academic, 1984).
- B. T. Miles, X. Hong, and H. Gersen, "On the complex point spread function in interferometric cross-polarisation microscopy," *Opt. Express* **23**, 1232–1239 (2015).
- K. Goda, A. Mahjoubfar, C. Wang, A. Fard, J. Adam, D. R. Gossett, A. Ayazi, E. Sollier, O. Malik, E. Chen, Y. Liu, R. Brown, N. Sarkhosh, D. Di Carlo, and B. Jalali, "Hybrid dispersion laser scanner," *Sci. Rep.* **2**, 445 (2012).
- T. Udem, J. Reichert, R. Holzwarth, and T. W. Hänsch, "Accurate measurement of large optical frequency differences with a mode-locked laser," *Opt. Lett.* **24**, 881–883 (1999).
- M. Niering, R. Holzwarth, J. Reichert, P. Pokasov, T. Udem, M. Weitz, T. W. Hänsch, P. Lemonde, G. Santarelli, M. Abgrall, P. Laurent, C. Salomon, and A. Clairon, "Measurement of the hydrogen 1S-2S transition frequency by phase coherent comparison with a microwave cesium fountain clock," *Phys. Rev. Lett.* **84**, 5496–5499 (2000).
- T. Udem, R. Holzwarth, and T. W. Hänsch, "Optical frequency metrology," *Nature* **416**, 233–237 (2002).
- K. Minoshima, H. Matsumoto, Z. Zhang, and T. Yagi, "Simultaneous 3-D imaging using chirped ultrashort optical pulses," *Jpn. J. Appl. Phys.* **33**, L1348–L1351 (1994).
- S. Xiao and A. M. Weiner, "2-D wavelength demultiplexer with potential for  $\geq 1000$  channels in the C-band," *Opt. Express* **12**, 2895–2902 (2004).

27. K. Oka and T. Kato, "Spectroscopic polarimetry with a channeled spectrum," *Opt. Lett.* **24**, 1475–1477 (2004).
28. S. Schiller, "Spectrometry with frequency combs," *Opt. Lett.* **27**, 766–768 (2002).
29. F. Keilmann, C. Gohle, and R. Holzwarth, "Time-domain mid-infrared frequency-comb spectrometer," *Opt. Lett.* **29**, 1542–1544 (2004).
30. T. Yasui, Y. Kabetani, E. Saneyoshi, S. Yokoyama, and T. Araki, "Terahertz frequency comb by multifrequency-heterodyning photoconductive detection for high-accuracy, high-resolution terahertz spectroscopy," *Appl. Phys. Lett.* **88**, 241104 (2006).
31. I. Coddington, N. Newbury, and W. Swann, "Dual-comb spectroscopy," *Optica* **3**, 414–426 (2016).
32. S. A. Diddams, L. Hollberg, and V. Mbele, "Molecular fingerprinting with the resolved modes of a femtosecond laser frequency comb," *Nature* **445**, 627–630 (2007).
33. M. Shirasaki, "Large angular dispersion by a virtually imaged phased array and its application to a wavelength demultiplexer," *Opt. Lett.* **21**, 366–368 (1996).
34. Y. Nakajima, H. Inaba, K. Hosaka, K. Minoshima, A. Onae, M. Yasuda, T. Kohno, S. Kawato, T. Kobayashi, T. Katsuyama, and F.-L. Hong, "A multi-branch, fiber-based frequency comb with millihertz-level relative linewidths using an intra-cavity electro-optic modulator," *Opt. Express* **18**, 1667–1676 (2010).
35. A. Nishiyama, S. Yoshida, Y. Nakajima, H. Sasada, K. Nakagawa, A. Onae, and K. Minoshima, "Doppler-free dual-comb spectroscopy of Rb using optical-optical double resonance technique," *Opt. Express* **24**, 25894–25904 (2016).
36. A. Asahara, A. Nishiyama, S. Yoshida, K. Kondo, Y. Nakajima, and K. Minoshima, "Dual-comb spectroscopy for rapid characterization of complex optical properties of solids," *Opt. Lett.* **41**, 4971–4974 (2016).
37. E. Baumann, F. R. Giorgetta, W. C. Swann, A. M. Zolot, I. Coddington, and N. R. Newbury, "Spectroscopy of the methane  $\nu_3$  band with an accurate midinfrared coherent dual-comb spectrometer," *Phys. Rev. A* **84**, 062513 (2011).
38. J. Roy, J.-D. Deschênes, S. Potvin, and J. Genest, "Continuous real-time correction and averaging for frequency comb interferometry," *Opt. Express* **20**, 21932–21939 (2012).
39. K. K. Tsia, K. Goda, D. Capewell, and B. Jalali, "Performance of serial time-encoded amplified microscope," *Opt. Express* **18**, 10016–10028 (2010).
40. X. Zhao, G. Hu, B. Zhao, C. Li, Y. Pan, Y. Liu, T. Yasui, and Z. Zheng, "Picometer-resolution dual-comb spectroscopy with a free-running fiber laser," *Opt. Express* **24**, 21833–21845 (2016).
41. Y. Liu, X. Zhao, B. Zhao, Z. Yao, G. Hu, T. Yasui, and Z. Zheng, "Broadband dual-comb spectroscopy with a polarization-multiplexed, dual-comb fiber laser," in *Fourier Transform Spectroscopy* (Optical Society of America, 2016), paper FM4D-2.
42. S. Mehravar, R. A. Norwood, N. Peyghambarian, and K. Kieu, "Real-time dual-comb spectroscopy with a free-running bidirectionally mode-locked fiber laser," *Appl. Phys. Lett.* **108**, 231104 (2016).
43. T. Ideguchi, T. Nakamura, Y. Kobayashi, and K. Goda, "Kerr-lens mode-locked bidirectional dual-comb ring laser for broadband dual-comb spectroscopy," *Optica* **3**, 748–753 (2016).
44. T. Ideguchi, A. Poisson, G. Guelachvili, N. Picqué, and T. W. Hänsch, "Adaptive real-time dual-comb spectroscopy," *Nat. Commun.* **5**, 3375 (2014).
45. K. Shibuya, T. Minamikawa, Y. Mizutani, H. Yamamoto, K. Minoshima, T. Yasui, and T. Iwata, "Scan-less hyperspectral dual-comb single-pixel imaging in both amplitude and phase," *Opt. Express* **25**, 21947–21957 (2017).
46. Y.-D. Hsieh, Y. Iyonaga, Y. Sakaguchi, S. Yokoyama, H. Inaba, K. Minoshima, F. Hindle, T. Araki, and T. Yasui, "Spectrally interleaved, comb-mode-resolved spectroscopy using swept dual terahertz combs," *Sci. Rep.* **4**, 3816 (2014).
47. N. B. Hébert, V. Michaud-Belleau, S. Magnan-Saucier, J.-D. Deschênes, and J. Genest, "Dual-comb spectroscopy with a phase-modulated probe comb for sub-MHz spectral sampling," *Opt. Lett.* **41**, 2282–2285 (2016).